# Evaluation of SAR-Based Sea State Parameters and Roughness Length Derivation Over the Coastal Seas of the USA

Abdalmenem Owda, Andrey Pleskachevsky, Xiaoli Guo Larsén, Merete Badger, Dalibor Cavar, and Charlotte Bay Hasager, *Member, IEEE*

***Abstract*—This article presents comprehensive validation of specific sea state parameters (SSPs) and synthetic aperture radar (SAR)-derived wind speeds ($u_{\mathrm{SAR}}$). The article introduces a novel approach to retrieving roughness length ($z_0$) based on wave steepness, following the retrieval of the short wavelengths necessary to estimate $z_0$. The SAR onboard the Sentinel-1 (S1) satellite that was used specifically in the interferometric wide swath mode (IW) data. The data were processed using the extended version of CWAVE (CWAVE_EX) algorithm for SSPs and CMOD5 for $u_{\mathrm{SAR}}$. CWAVE_EX was developed especially for coastal waters; the processing chain includes steps for SAR image denoising and eliminating image artifacts. SAR S-1 data inherently exhibit a substantial azimuthal cutoff length due to the data's high satellite altitude and SAR IW resolution. That complicates the retrieving of short wavelengths prevalent in coastal zones and needed to retrieve $z_0$. The article focuses on the coastal seas of the USA, benefiting from the presence of an extensive network of ocean buoys for validation purposes. The complete SAR S1 A/B archive from 2014 to 2022 was first processed to retrieve SSPs and $u_{\mathrm{SAR}}$. The validation for significant wave height ($H_s$), second moment wave period ($T_{m2}$), and $u_{\mathrm{SAR}}$ was performed using in-situ measurements with about 6000 collocations. $H_s$ and $T_{m2}$ were compared against the corresponding parameters from hindcast spectral numerical model data with about 380 000 collocations. The comparisons between the retrieved $H_s$ and $T_{m2}$ against the in-situ observations and hindcast wave model data yielded a root mean square error (RMSE) of 0.46–0.50 m and 0.9–1.1 s. The RMSE of $u_{\mathrm{SAR}}$ against in-situ observation was about 2 m/s with a bias of 0.78 m/s. The estimated $z_0$ values from satellite-driven wave parameters were highly correlated with the $z_0$ estimated from the in-situ observations, with an RMSE of $0.04 \times 10^{-3}$ m and a bias of $-0.01 \times 10^{-3}$ m. The article highlights the possibility of using SAR remote sensing data for global mapping of $z_0$, including coastal effects of local variability in sea state and wind field gustiness.**

***Index Terms*—Air–sea interaction, extended version of CWAVE (CWAVE_EX), geophysical model function (GMF), integrated sea state parameter (SSP), Joint North Sea Wave Project (JONSWAP), neutral stratified wind, roughness length, synthetic aperture radar (SAR).**

Manuscript received 13 December 2023; revised 10 March 2024; accepted 17 April 2024. Date of publication 25 April 2024; date of current version 8 May 2024. The work of Abdalmenem Owda was supported by the European Union Horizon 2020 research and innovation program under Grant 861291 as part of the Train2Wind Marie Skłodowska-Curie Innovation Training Network (https://www.train2wind.eu/). A part of this work related to using the CWAVE_EX algorithm was supported by the German Aerospace Center at the Maritime Safety and Security Lab in Bremen. *(Corresponding author: Abdalmenem Owda.)*

Abdalmenem Owda, Xiaoli Guo Larsén, Merete Badger, Dalibor Cavar, and Charlotte Bay Hasager are with the DTU Wind and Energy Systems—Technical University of Denmark, 4000 Roskilde, Denmark (e-mail: abow@dtu.dk; xgal@dtu.dk; mebc@dtu.dk; daca@dtu.dk; cbha@dtu.dk).

Andrey Pleskachevsky is with the Maritime Safety and Security Lab, German Aerospace Center, 28359 Bremen, Germany (e-mail: andrey.pleskachevsky@dlr.de).

Digital Object Identifier 10.1109/JSTARS.2024.3393862

## I. Introduction

### A. Sea State Parameters Based on SAR in the Coastal Zones

SEA surface modulation induced by wind, commonly called "sea state," can be described by sea state parameters (SSPs), such as wave height, wavelength, wave period, and propagation direction. Comprehensive knowledge about sea states is crucial for various applications, including oceanography, maritime surveillance, climate models, and activities like constructing offshore installations, such as wind farms [1], [2]. SSPs influence the design, safety, reliability, power production, maintenance operations, and insurance and financing of floating offshore wind turbine projects [3]. Monitoring SSPs is essential but challenging in the harsh environment at sea and sea state variability of the coastal zones. SSPs can be observed in real-time using marine observations and monitoring infrastructures, such as ocean buoys and research platforms. However, there is a limitation regarding this technique as the buoys provide measurements at specific points. Forecasting, waves, and service models can provide SSPs with a limitation, as model outputs depend on other additional data inputs [1].

Synthetic aperture radar (SAR) spaceborne satellites are active microwave systems that operate independently of weather conditions, daytime, and cloud coverage. SAR provides large-scale snapshots of two-dimensional observations for the globe, offering unique advantages of retrieving wind and wave data compared to other remote sensing techniques. The rapid growth of the SAR archive, attributed to the increased deployment of SAR constellations and space missions, significantly enhances the utilization of SAR wind and wave data for various oceanic and atmospheric applications. SAR observations of the ocean surface enable mapping integrated SSPs over large areas spanning hundreds of kilometers in near-real-time [4], [5], [6].

Several articles showed the reliability of high-resolution SAR data for retrieving SSPs in open ocean and coastal areas [5], [6], [7], [8]. SSPs were retrieved based on converting SAR subscenes into an image spectrum using, for example, the fast-Fourier transformation (FFT). The CWAVE is one of the

algorithms that was initially developed for the open oceans to retrieve SSPs, including significant wave height ($H_s$) and second moment wave period ($T_{m2}$) [9]. An extended version of CWAVE (CWAVE_EX) has more features than CWAVE, aiming to enhance its suitability in coastal zones [10]. CWAVE_EX algorithm was tuned and validated using two independent wave models: WaveWatch-3 [National Oceanic and Atmospheric Administration (NOAA)] and Copernicus Marine Environment Monitoring Service (CMEMS), as well as National Data Buoy Center (NDBC) marine observations.

The use of SAR data in the coastal zones poses a challenge due to several factors: 1) the complexity of surface wave dynamics in the coastal zones, and 2) SAR data can be affected by oceanic effects that are not related to wind data, such as shoaling effects caused by bathymetry [10]. Furthermore, the type of SAR data used plays an important role in the reliability and accuracy of SSPs. As higher resolution SAR data are used, more accurate results can be achieved. Consequently, one research gap of the article is to comprehensively validate SSPs based on SAR interferometric wide swath (IW) data in the coastal zones. This research gap is still critical to be addressed [8], particularly the algorithms used to retrieve SSPs and wind speeds for coastal areas.

### B. Roughness Length Retrieval Based on Wave Steepness After Overcoming Cutoff Effects

The presence of reliable SAR SSPs plays a crucial role in calculating additional parameters essential for advancing oceanic and atmospheric applications, particularly in the offshore wind industry. Roughness length ($z_0$) plays a crucial role in dynamic momentum and heat exchange between the atmosphere and ocean [11], [12]. $z_0$ is a vital parameter for accurately estimating the vertical structure of the wind profile at offshore wind farms sites [13]. There usually needs to be more information about $z_0$ for climate numerical modeling and forecasting [8]. $z_0$ can be described by the Charnock equation [14], which was first derived for fully developed waves associated with deep and open waters. Measurements have been applied to derive an empirical representation of $z_0$, including in-situ masts, buoys, ships, wave tank experiments, and sounding data [15]. Several schemes have been derived for estimating $z_0$ using integrated SSPs, such as wave age, wavelength at peak frequency, wave steepness, and wave height [16], [17].

The wave steepness represents the ratio of $H_s$ to the peak wavelength ($L_p$). The wavelengths are typically shorter in the coastal zones compared with the open oceans. This, in turn, requires higher resolution SAR data that can map the short wavelengths, which is not the case in this article. The SAR IW resolution and high satellite altitude of Sentinel-1 (S1) A/B intensify the complexity of mapping short wavelengths [1]. The periodic displacement of surface waves, especially their movement toward the radar, leads to stretching and bunching image intensities in the azimuth direction, known as velocity bunching. Therefore, azimuthal traveling waves shorter than a specific threshold remain invisible to imagining. This phenomenon is known as cutoff effects in the sea state imaging process [18]. Therefore, the short wavelengths fall within the cutoff length. To estimate $z_0$ based on wave steepness, the article intends to introduce a method to overcome the cutoff effects based on the combination of SSPs and the empirical Joint North Sea Wave Project (JONSWAP) model.

In summary, the main objectives of the article are to 1) investigate the potential and limitations of SAR IW data for retrieving wind and wave data in the coastal zones, and 2) present an approach to overcome the limitations associated with cutoff effects, aiming to retrieve $z_0$ in the coastal zones based on wave steepness.

The rest of this article is organized as follows. Section II presents the study area and dataset used. In Section III, the methodology is demonstrated. The results and discussion are shown in Sections IV and V, respectively. Finally, Section VI concludes this article.

TABLE I
GEOGRAPHIC DETAILS OF EACH STUDY AREA, INCLUDING THE NUMBER OF BUOYS AVAILABLE AND WAVE AND WIND COLLOCATED SAMPLES WITH SENTINEL-1 A/B

| Study area ID | Geographic details (longitude and latitude) | NDBC buoys | Number of collocated samples (wave) | Number of collocated samples (wind) |
|---|---|---|---|---|
| **Atlantic** | (67°W – 82°W), (30°N – 42°N) | 20 | 3786 | 719 |
| **Gulf of Mexico** | (82°W – 97°W), (22°N – 30°N) | 12 | 1165 | 611 |
| **Pacific** | (117°W – 137°W), (31°N – 46°N) | 42 | 5639 | 3882 |

## II. STUDY AREA, DATASET, AND COLLOCATION

### A. Study Areas

Three study areas along the coastlines of the USA were chosen, and these areas have plenty of in-situ measurements of waves and winds (Fig. 1). Table I presents the geographic location and number of buoys for each study area and the number of corresponding SAR collocation of each study area.

### B. Datasets and Collocation

*1) Satellite SAR Data:* The C-band satellite SAR data from European Space Agency missions S1-A and S1-B were used in this article. They both operate at an altitude of 704 km with a 6-day repeat cycle. The most available acquisition mode for the study areas is the IW mode. The individual IW mode (ground range detected high-resolution products-level 1) uses three subswaths, covering approximately 250 km in range and 200 km in azimuth with a pixel spacing of 10 m. IW mode has various polarization options (dual HH + HV, VV + VH, single HH, and VV). For sea state estimation, the priority is given to VV polarization due to its sensitivity to surface roughness caused by wind and waves. Zhang et al. [19] showed that VV polarization is more suitable than HH for wind surface velocity.

*2) In-Situ Measurements:* Ocean buoy observations from the USA NDBC, operated by the NOAA, were used in the validation. The buoys are distributed in water depths ranging from 25 to

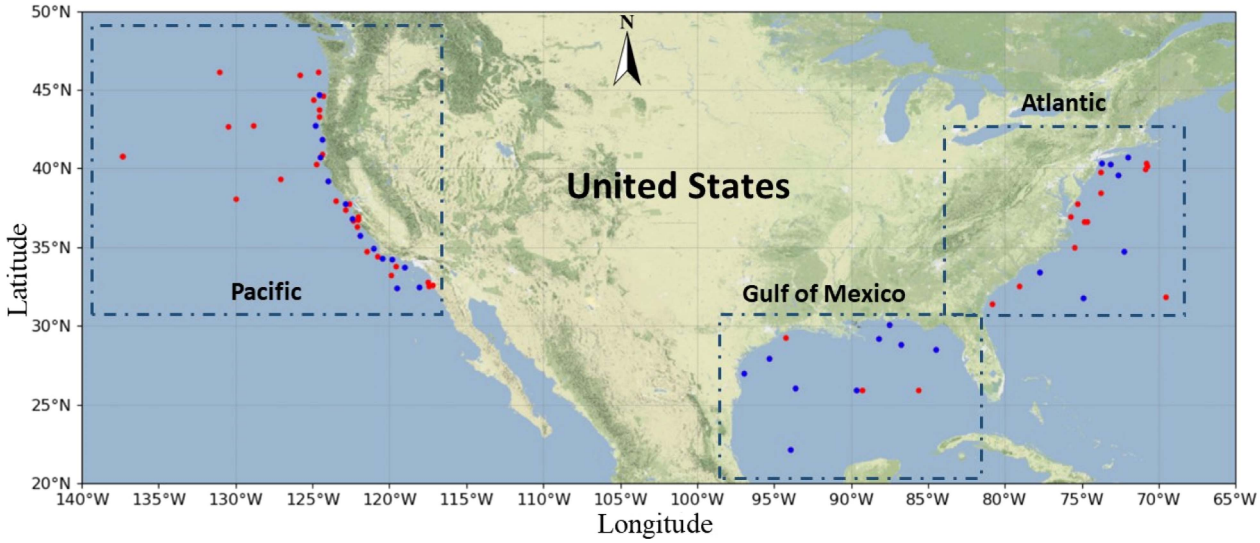


Fig. 1. Three study areas with the location of NDBC ocean buoys. Red- and blue-marked buoys provide wave data. Blue-marked buoys provide wind data speed.

4500 m and distances to the coastline from 13 to 400 km. The following are the measurements involved in the validation and computation steps.

a) The measurements of $H_s$ and average wave period from ocean buoys were used to validate both $H_s$ and $T_{m2}$ from S1 IW scenes.
b) The dominant wave period measurements (DPD) and water depth were utilized to estimate the peak wavelength ($L_p$) using dispersion relation (17). When DPD from ocean buoy measurements is used to estimate $L_p$, it is denoted as $L_{p\_\mathrm{NDBC}}$. $L_{p-S1\ \mathrm{IW}}$ also refers to $L_p$ but estimated using SAR SSPs.
c) The reference wind speed measurements ($u_{\mathrm{reference}}$) are available for an average of 10 min and were used to validate SAR-derived wind speed ($u_{\mathrm{SAR}}$).

*3) Météo-France WAve Model (MFWAM) From Copernicus Marine Environment Monitoring Service (CMEMS) Data:* Météo-France WAve Model (MFWAM)–CMEMS is a hindcast spectral numerical model wave data with a resolution of 1/12 degree. MFWAM is simulated wave data resulting from running a third generation of MFWAW. The results are provided in 3-hourly steps. MFWAW is a wave forecast model that provides wind and wave data as grid point analysis and forecast field. It is operated by Météo-France [20] and is free to access.

*4) Collocations and Data Filtering:* The available S1 A/B IW scenes were temporally and spatially collocated over the buoy locations of the study areas. For the complete S1 IW archive from 2014 to 2022, approximately 2900 SAR scenes were collocated with wind–wave buoys, resulting in around 10 500 and 5200 wave and wind collocations, respectively. The collocations were identified in the three study areas listed in Table I.

Out of the total 74 NDBC buoys, it was found that they were spatially collocated with S1 IW scenes and positioned inside the subscenes. S1 IW scenes were synchronized in time with measurements taken by ocean buoys. The closest buoy measurement served as the reference point in time. Bilinear interpolation was applied to certain observations to account for discrepancies between the SAR scene's recorded time and the buoy measurements. However, the number of buoys involved in $H_s$ and $T_{m2}$ validation was reduced to 54 due to some buoys' time gaps in their measurements. The time gaps ranged from a few hours to days and sometimes for months. Within the study period, 44 of the 54 buoys were equipped with an anemometer to measure wind speed.

Regarding SAR SSP collocations with MFWAM data, the SAR SSPs from the archive of the year 2020, covering the Atlantic and Gulf of Mexico, were bilinearly collocated both spatially and temporally with MFWAM data, generating about 380 000 collocations. S1 IW scenes were processed with a raster of 2.5 km. The MFWAM outputs were bilinear and interpolated spatially for the exact geolocation of the collocated subscene center. The same method of temporal collocation used for ocean buoys was also applied to MFWAM data.

Only $H_s$ values exceeding 10 m were filtered out to ensure data validity. It is important to note that the buoys are susceptible to overturning in extreme wave conditions, introducing uncertainty regarding the reliability of reference measurements. The buoys or platforms could not measure wave parameters in extreme wave conditions [21].

## III. Method

The proposed methodology of the two main research objectives of the article is described in the following sections. Section III-A demonstrates the stages of retrieval of SSPs (III-A-1), wind speeds (III-A-2), and method of validation and comparison for SSPs and wind speed measurements (III-A-3). Section III-B presents the workflow used to retrieve roughness length based on wave steepness after overcoming the cutoff effects, including an explanation of cutoff effects (III-B-1), overcoming the cutoff effects based on the JONSWAP model and

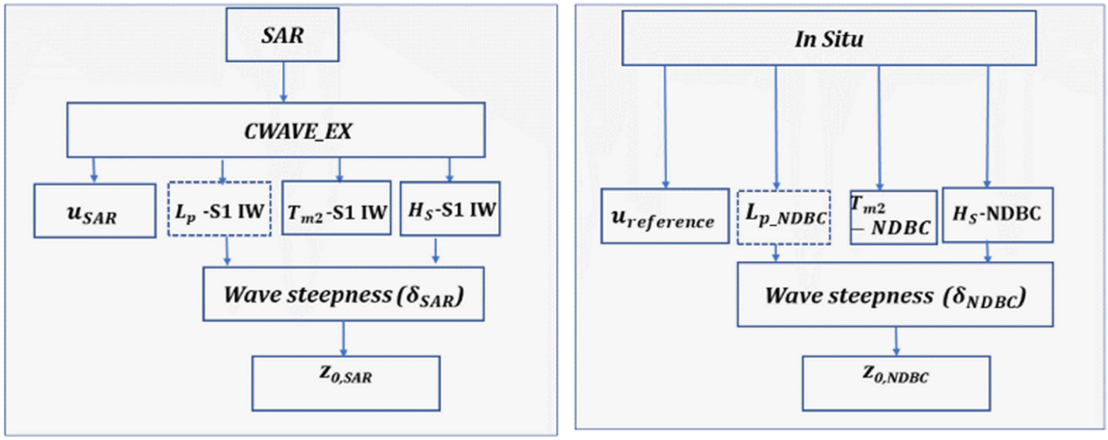


Fig. 2. Workflow diagram of the study. The full line rectangles indicate parameters derived by CWAVE_EX (left panel) and buoy data (right panel). The dashed rectangles indicate a parameter estimated by additional computation due to its nonavailability directly (illustrated in Section III-B-1).

SSPs from CWAVE_EX (III-B-2), and estimation of roughness length (III-B-3-4).

Fig. 2 illustrates the workflow for obtaining the derived SSPs, reference measurements, and the involved parameters in the computation and calibration of $z_0$, derived from two main instruments: the ocean buoy and the SAR sensor of S1 A/B satellites. When $z_0$ is estimated from in-situ measurements or satellite measurements, it denoted as $z_{0,\mathrm{NDBC}}$ or $z_{0,\mathrm{SAR}}$, respectively.

### A. Sea State Parameters and Wind Speeds Based on S1 IW in the Coastal Zone

*1) Retrieval of Integrated SSP From S1 IW:* When a breeze blows over the sea's smooth surface at 2–3 m/s or more, it quickly disturbs the water's surface layer, forming capillary and short-gravity waves [22]. The radar detects echoes primarily caused by "Bragg-scattering" of capillary waves. The recorded backscattered signals form images of the normalized radar cross section (NRCS), representing the sea surfaces' ability to return radar signals. The rougher the sea surface, the more energy is returned to the radar instrument. NRCS (or $\sigma_0$) is generally accepted as the fundamental parameter for retrieving wind and wave data [8], [23]. S1 $\sigma_0$ is computed according to [24], as follows:

$$\sigma_0 = \frac{|\mathrm{DN}_i|^2}{A_{\mathrm{dn}}^2 K} \tag{1}$$

where $\mathrm{DN}_i$ is the digital number at the location $i$, $A_{\mathrm{dn}}$ is the pixel scaling, and $K$ is the absolute calibration factor provided with S1 L1 as a calibration grid.

The CWAVE_EX algorithm was utilized for estimating a series of integrated SSPs, including significant wave height ($H_s$), dominant ($H_s^{\mathrm{swell}-1}$) and secondary swell ($H_s^{\mathrm{swell}-2}$), windsea wave heights ($H_s^{\mathrm{wind}}$), first ($T_{m1}$) and second moment, wave periods ($T_{m2}$), mean wave period ($T_m$), and period of wind sea ($T_s^{\mathrm{wind}}$). The algorithm involves several data preparation steps, including 1) SAR scene reading, calibration, and land masking, 2) subscene preparation and filtering outliers (e.g., ships, ship wakes, oil spills, etc.), 3) image power spectra were created by applying FFT window (1024 × 1024 pixel) to the resampled pixels (each pixel is split into 4 × 4 = 16 pixels); therefore, the modified pixel resolution is 2.5 m instead of 10 m, 4) integrated energy parameters were computed from image power spectra and by integration along directions of satellite image and flight for wave number domain 0.003–0.21 (equivalent to wavelength 2000 to 30 m) [6], and 5) all features estimated from the SAR scene and additional introduced SAR features, such as texture analysis (e.g., grey level co-occurrence matrix) to extract feature analysis parameters used for retrieving integrated SSPs. Table II in [23] presented all SAR features used as input for the CWAVE_EX model.

*2) Wind Retrieval From SAR:* NRCS is related to the local near-surface wind speed through a geophysical model function (GMF). In the context of this article, the CMOD5 GMF is used to retrieve the wind speed at 10 m a.m.s.l, which is implemented in the CWAVE_EX algorithm. The general equation of CMOD5 is

$$\sigma_0 = \mathrm{CMOD}\ (c, v, \emptyset, \theta) = B_0\ (c_0, v, \theta)\,[1 + B_1\,(c_1, v, \theta) \times \cos\emptyset + B_2\,(c_2, v, \theta)\cos(2\emptyset)]^p \tag{2}$$

where $v$ is the 10 m stability-dependent wind speed; henceforth $u_{\mathrm{SAR}}$, $\emptyset$ is the angle between the wind direction and the azimuth look angle of the SAR (both measured from the north), and $\theta$ is the radar incidence angle. The other coefficients $c_i$ shape the terms $B_i$, and $p$ is a constant with a value of 1.6 [25]. To retrieve $u_{\mathrm{SAR}}$, (2) is inverted and complementary information on the wind direction as input to GMF is required [26]. The wind direction is taken from a global forecasting system model and interpolated to the corresponding SAR acquisition time.

SAR IW level 1 already has a reduced speckle noise with an equivalent number of looks set at 4.5. Before retrieving $u_{\mathrm{SAR}}$, several stages of filtering were implemented in the algorithm to filter out the high and low NRCS with an object size of 200 m (equivalent to ship size), wind farms, oil spills, and algae. A spatial average filter with a 500 m size is further applied to SAR IW before $u_{\mathrm{SAR}}$ retrieval process, aiming to reduce additional speckle noise. $u_{\mathrm{SAR}}$ were retrieved from SAR wind maps through

a rectangle bin of 2.5 km × 2.5 km. The local wind speeds are one of the primary features for extracting SSPs. Therefore, CMOD5 is a part of the CWAVE_EX algorithm.

*3) Method for Validation and Comparison of Integrated Sea State Parameters:* The integrated SSPs were validated against ocean buoy observations for $H_s$ and $T_{m2}$. These two parameters are relevant for a series of technical applications [27] and are used for calculating $z_0$ (see Section III-B-4). About 6700 out of 10 500 collocations were available for validation due to the reasons and criteria mentioned in Section II-B-4. The S1 IW scenes were processed using a 2.5 × 2.5 km raster and $H_s$ and $T_{m2}$ were compared with the corresponding time measurements of the same parameters from NDBC buoys. The maximum time resolution used is 1 h at maximum.

The most collocations were found for the buoy 46 011, which covers the period between 2020 and the middle of 2022. The time series of SAR observations and their corresponding in-situ measurements of this buoy are presented in Fig. 4 in Section IV-A.

$H_s$ and $T_{m2}$ derived from SAR were compared with MFWAM–CMEMS data according to the method explained in Section II-B-4.

### *B. Roughness Length Estimation Based on the Wave Steepness Concept and Overcoming the Cutoff Effects*

*1) Cutoff Effects:* The azimuthal cutoff is an inherent disadvantage of SAR. The waves shorter than the cutoff length cannot be imaged directly by SAR [28]. Holt introduced a simple empirical formula to estimate the minimum visible wavelength for azimuthal traveling waves ($L_{\min}$) [29]. The empirical formula depends on the geometry of the satellite and $H_s$

$$L_{\min} = C_0 \frac{R_0}{V_{\text{SAR}}} H_S^{0.5} \tag{3}$$

where $R_0$ is the slant range (ca 9.2 × $10^5$ m for S-1), $V_{\text{SAR}}$ is the velocity of the SAR satellite (6.8 km/s for S-1), and $C_0$ is a constant of order 1 (unit: $\text{m}^{0.5} \times \text{s}^{-1}$).

Based on the (3) at $H_s = 1$ m, it yields $L_{\min} \sim 135$ m [1]. S1 data inherently possesses a higher cutoff length than satellites operating at lower altitudes.

*2) Peak Wavelength Estimation Using JONSWAP Spectrum and Dispersion:* The short wavelengths (less than 135 m) cannot be mapped in S1 IW images due to the cutoff by the sea state imaging process. To obtain short $L_p$, the JONSWAP spectrum model was utilized. JONSWAP spectrum is the outcome of applying peak control factor to the *Pierson–Moskowitz* spectrum to improve the fit of collected wave observations of JONSWAP by Hasselmann et al. [30]. JONSWAP spectrum was proposed using the existing Philips parameters and peak wave frequency ($f_p$). The JONSWAP spectrum model is given in the angular frequency $\omega$ domain

$$S\ (w) = \frac{\alpha g^2}{w^5} \exp^{\left[\frac{-5}{4}\ \left(\frac{w_p}{w}\right)^4\right]} \gamma^{\exp\left[-\frac{(w-w_p)^2}{2\sigma^2 w_p^2}\right]} \tag{4}$$

$$\alpha\ =\ 0.076\left(\frac{U_{10}^2}{Fg}\right)^{0.22} \tag{5}$$

$$w_p =\ 22\left(\frac{g^2}{U_{10}F}\right)^{\frac{1}{3}} \tag{6}$$

$$\sigma = \begin{Bmatrix} 0.07,\ for\ w \leq\ w_p \\ 0.09,\ for\ w \geq\ w_p \end{Bmatrix}$$

where $S(w)$ is the wave spectral density ($\text{m}^2$/Hz), $\alpha$ is the Philips parameter, $w_p$ is the angular peak frequency, $w$ is the angular frequency, $\gamma$ peak control factor and is 3.3, $F$ is the fetch distance, $g$ is the gravitational acceleration, and $U_{10}$ is the wind speed at 10-m level.

The JONSWAP model is introduced to reproduce SSPs generated by the CWAVE_EX algorithm, referred to as JONSWAP SSPs. This process is iterative and controlled by increments of $f_p$ and $F$. The disparities between JONSWAP SSPs and CWAVE_EX SSPs are calculated in each iteration. The $f_p$ is selected from the iteration that exhibits the lowest differences between both sets of SSPs.

The JONSWAP model was considered on a range of angular wave frequencies from 0 to $2\pi$ Hz and for various fetch distances ranging from 20 to 150 km. The threshold of 0.125 Hz (corresponds to 8 s period) was applied for participation in the spectrum for swell and wind sea parts. The statistical *n*-order momentum of the spectrum in the frequency domain can be obtained by integrating the energy over the wave spectrum

$$m_n = \int_{f=0}^{f=1} S\,(f)\, f^n df \tag{7}$$

where $S(f)$ is the wave spectral density in the frequency domain, and $f$ is the frequency range of the waves between 0 and 1 Hz. The following integrated SSPs have been computed [8], [31]:

$$H_s =\ 4\sqrt{m_0} \tag{8}$$

$$H_{s,}^{\text{swell}-1} =\ 4\sqrt{m_{0,\text{swell}}} \tag{9}$$

$$H_s^{\text{wind}} =\ 4\sqrt{m_{0,\ \text{sww}}} \tag{10}$$

$$T_m = \frac{m_{-1}}{m_0} \tag{11}$$

$$T_{m1} = \frac{m_0}{m_1} \tag{12}$$

$$T_{m2} = \sqrt[2]{\frac{m_0}{m_2}}\ . \tag{13}$$

The peak frequency is estimated by minimization of an error

$$\sigma\ = \sqrt{\sum\nolimits_{i=0}^{i=n} (\sigma_i)^2} \to 0 \tag{14}$$

where $\sigma_i$ means differences of SSPs estimated from JONSWAP and CWAVE_EX SSPs, *i* means the parameter number, e.g., for $i = 1$ $\sigma_1 = H_s^{\text{JONSWAP}} - H_s^{\text{CWAVE\_EX}}$, and $n$ is the number of parameters, $n = 6$.

SSPs of the CWAVE_EX algorithm include two swell components, namely dominant and secondary systems. As JONSWAP cannot separate these two components, the total swell wave height was estimated from S1 IW

$$H_s^{\text{Swell}} = \sqrt{(H_s^{\text{Swell}-1})^2 + (H_s^{\text{Swell}-2})^2}\ . \tag{15}$$

The advantage of this approach is that six parameters can be compared in total ($H_s$, $T_m$, $T_{m1}$, $T_{m2}$, $H_s^{\text{swell}-1}$, and $H_s^{\text{swell}-2}$).

The dispersion relation relates the wave properties wavelength, frequency, and depth. The following dispersion formula is used to compute $L_p$ based on the computed peak frequency $f_p$

$$w_p{}^2 = gk \tan h\,(kh) + c \tag{16}$$

where $w_p$ is the angular peak frequency $w_p = \frac{2\pi}{T_p}$, $g$ is gravitational acceleration, $k$ is the wavenumber $k = \frac{2\pi}{L_p}$, $h$ is water depth, and $c$ is the component of the surface currents in wave propagation direction and is negligible. By substituting $w_p$ and $k$ into (16), it leads to the following equation with only one unknown, which is $L_p$:

$$\left(\frac{2\pi}{T_p}\right)^2 = g\frac{2\pi}{L_p} \tan h\left(\frac{2\pi}{L_p}h\right). \tag{17}$$

Based on the calculated $T_p$ and the water depth ($h$) under each buoy station, the peak wavelength ($L_p$) is estimated from the dispersion relation in (17), denoted $L_{p-S1\ \text{IW}}$.

Ocean buoys provide measurements of the DPD (DPD $= T_p = \frac{1}{f_p}$), representing the period with the maximum wave energy. $L_p$ estimated from DPD measurements based on dispersion relation is denoted as ($L_{p\_\text{NDBC}}$). $L_{p-S1\ \text{IW}}$ and $L_{p\_\text{NDBC}}$ were involved in measuring $\delta$ alongside $H_{S-S1\ \text{IW}}$ and $H_{S-\text{NDBC}}$, to estimate $z_{0,\text{SAR}}$ and $z_{0,\text{NDBC}}$, respectively (see Fig. 2).

*3) Estimation of Wind Speeds Using the Logarithmic Wind Profile:* The logarithmic wind profile describes how the wind speed varies with height and is used to compute wind speeds using calibrated $z_{0,\text{NDBC}}$ ($u_{z0,\text{NDBC}}$). The mathematical representation is as follows:

$$u_z = \frac{u_*}{k}\left[\ln\left(\frac{z}{z_0}\right) + \varphi\right] \tag{18}$$

where $u_z$ (m/s) is the wind speed at the height $z$ (m), $u_*$ is the friction velocity (m/s), $z_0$ is the roughness length (m), $k$ is the Von Kármán constant of 0.4, and $\varphi$ is the stability correction term. Assuming neutral stability, which means $\varphi$ is zero. The Charnock formulation has been widely used in various articles [32], [33], [34], [35] to estimate $u_*$ as a function of the $z_0$ as follows:

$$u_* = \sqrt{\frac{g \times z_0}{\alpha_{\text{ch}}}} \tag{19}$$

where $\alpha_{ch}$ is Charnock's coefficient, which is 0.0144 by Garratt's review [35] and $g$ (m/s$^2$) is the gravitational acceleration. Several articles proposed different values for Charnock parameters, e.g., Liu et al. [36] have shown values of the Charnock constant from different research based on various laboratory and field observations in Table I of their article.

*4) Roughness Length Calculation:* The steepness of the waves ($\delta$) is a commonly used parameter to describe the air–sea interface with the development of the wind waves, as it characterizes the physical roughness of the sea surface. $\delta$ is defined as the ratio between $H_S$ and $L_p$[38]

$$\delta = \frac{H_S}{L_p} \tag{20}$$

where $\delta$ is often applied in the wave parametrization of the momentum transfer. Several wave-dependent surface roughness parametrizations have been derived theoretically and experimentally in the field or the laboratory. Among these, widely cited schemes based on $\delta$ include 1) Anctile and Donelan [37], 2) Taylor and Yelland [17], and 3) Takagaki et al. [38]. These schemes can be generally formulated as follows:

$$\frac{z_0}{H_s} = \alpha\delta^\beta \tag{21}$$

where $\alpha$ and $\beta$ are the schema parameters derived from the wind conditions of the experiments or field data. The coefficients $\alpha$ and $\beta$ have been derived for specific locations and may not fit well with all wind conditions in the investigated areas, e.g., wind direction and fetch distance. Therefore, a correction factor ($\gamma > 0$) was introduced to calibrate the scheme and to obtain a suitable $z_0$ for our sites, ensuring that wind speeds $u_{z0,\text{NDBC}}$ estimated from those modified $z_{0,\text{NDBC}}$ had the lowest root mean square error (RMSE) and bias when compared to $u_{\text{reference}}$. Consequently, the modified version of the roughness scheme can be formulated as follows:

$$z_0 = \gamma(H_s\ \alpha\delta^\beta). \tag{22}$$

This modification is necessary to extrapolate $u_{\text{reference}}$ at the level of $u_{\text{SAR}}$ using (16) and (17).

## IV. Results

### A. Integrated Sea State Parameters and Wind Speeds

The integrated SSPs $H_s$ and $T_{m2}$ were retrieved from three sources: in-situ buoy data, MFWAM–CMEMS, and CWAVE_EX data derived from SAR.

First, the CWAVE_EX wave data were validated to buoy data as reference [Fig. 3(a) and (b)]. The results indicated that CWAVE_EX $H_s$ exhibited a slight negative bias (−0.05 m) and RMSE 0.54 m, while CWAVE_EX $T_{m2}$ showed no bias and RMSE 1.28 s. It has been found that numerous points of CWAVE_EX $T_{m2}$ underestimate the reference measurements, which is not the case for CWAVE_EX $H_s$. The correlation coefficient was higher for CWAVE_EX $H_s$ ($R = 0.82$) compared with CWAVE_EX $T_{m2}$ ($R = 0.69$).

Next, the MFWAM–CMEMS model results on $H_s$ and $T_{m2}$ were compared with the CWAVE-EX wave data [see Fig. 3(c) and (d)]. In this case, $H_s$ showed no bias, as the algorithms tuned originally with model data, and RMSE at 0.46 m, while $T_{m2}$ exhibited a bias at 0.49 s and RMSE at 0.94 s. The correlation coefficients were higher for $H_s$ ($R = 0.82$–$0.86$) than for $T_{m2}$ ($R = 0.72$–$0.75$) in both comparisons.

The wind speed ($u_{\text{SAR}}$) derived from SAR by CMOD5 GMF was validated to $u_{\text{reference}}$ and the result is shown in Fig. 3(e). The linear correlation statistics showed an RMSE of ∼2.0 m/s, a bias of 0.78 m/s, and an $R$ of 0.85.

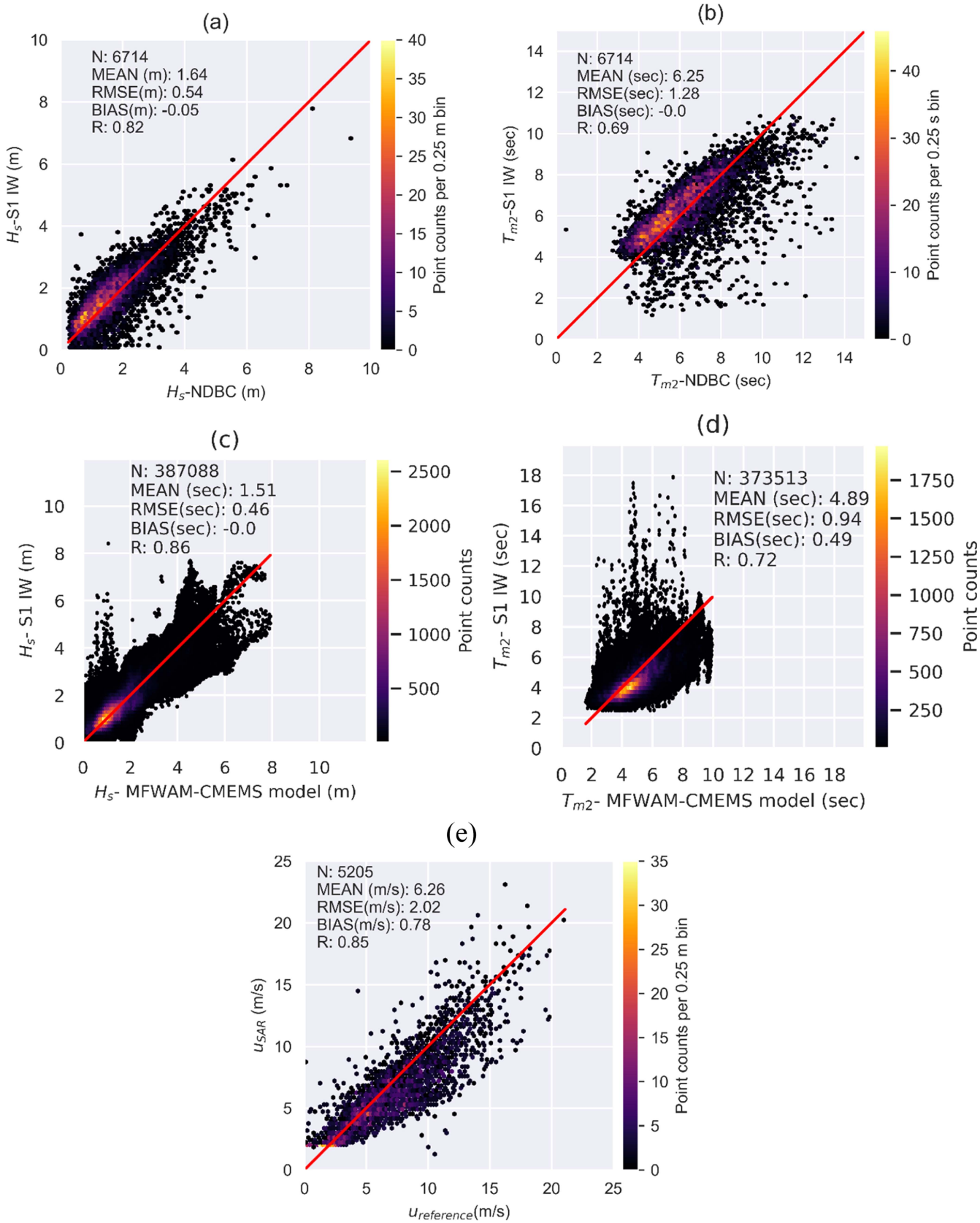


Fig. 3. CWAVE_EX validation and comparison results. (a) Significant wave height ($H_s$) validation from S1 IW against $H_s$ from NDBC. (b) Mean second moment wave period ($T_{m2}$) from S1 IW against mean wave period (APD) from NDBC. (c) $H_s$ from CMEMS model against $H_s$ from S1 IW. (d) $T_{m2}$ from CMEMS model against $T_{m2}$ from S1 IW. (e) SAR-derived wind ($u_{\mathrm{SAR}}$) vs. extrapolated reference wind speed ($u_{\mathrm{reference}}$).

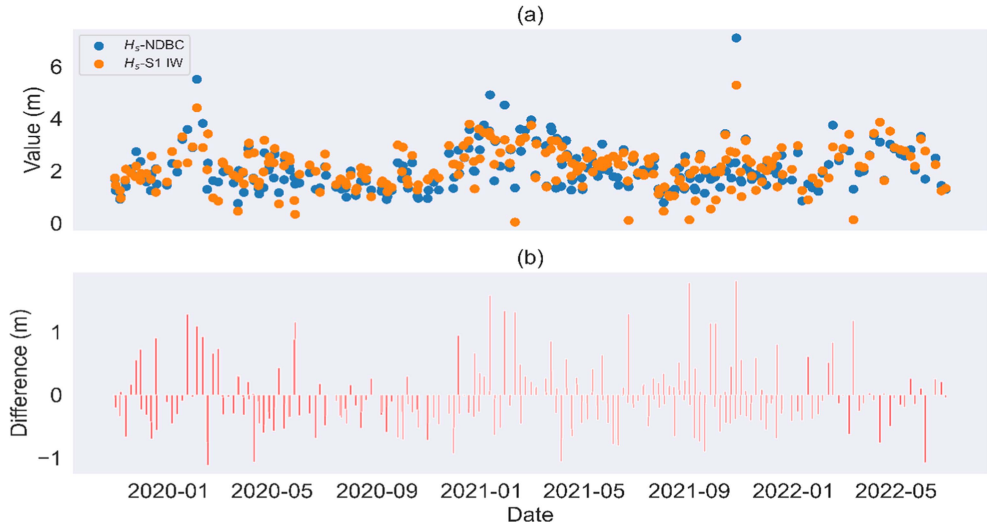


Fig. 4. Time-series record of $H_s$ from ocean buoys ($H_s$ – NDBC) and CWAVE_EX ($H_s$ – $S1$ IW) for the buoy 46 011 ($N = 480$ collocations).

The time-series analysis of $H_s$, their corresponding in-situ measurements, and their differences from buoy 46 011 in the Pacific were presented in Fig. 4(a) and (b) with 480 collocations. $H_s$ based on SAR showed good agreement with buoy data in Fig. 4(a) except in some cases. It was noticed in Fig. 4(b) that the uncertainties in $H_s$ from CWAVE_EX increased for high $H_s$ values larger than 5 m, with absolute differences ranging between 1 and 1.5 m. The temporal resolution of the time series is 6 and 12 days for observations before and after 2021, respectively.

### *B. Roughness Length Retrieval Based on Wave Steepness After Overcoming Cutoff Effects*

*1) Overcoming Cutoff Effects Based on JONSWAP, CWAVE_EX SSPs, and Dispersion:* $T_p$ $\left(=\frac{1}{f_p}\right)$ alongside water depth are fundamental parameters to retrieve $L_p$ as illustrated in the (17), denoted $L_{p-S1\text{ IW}}$. Fig. 5 shows the estimated $T_p$ as a function of $T_{m2}$. The relationship is approximately linear with a best fit of $T_p = 0.79\, T_{m2} + 4.17$. This fit can potentially be used to estimate $T_p$ for any area independently of ocean buoy observations. The ratio between average values of $T_p$ and $T_{m2}$ in this article was 1.5.

*2) Roughness Length Scheme Calibration:* $u_{z0,\text{NDBC}}$ was estimated based on calibrated roughness length, aiming to find the lowest RMSE between $u_{z0,\text{NDBC}}$ and $u_{\text{reference}}$. The calibrated roughness length was estimated based on (22). The RMSE variation as a function of the correction factor $\gamma$ is demonstrated in Fig. 6(a). The smallest RMSE is found to be with $\gamma = 1.35$ and the parameters from the Takagaki schema ($\alpha = 10.94$ and $\beta = 3$). Fig. 6(b) shows the relationship between $u_{z0,\text{NDBC}}$ and $u_{\text{reference}}$ for the sample, after applying $\gamma = 1.35$.

*3) Roughness Length Calculation:* The computed values of $z_{0,\text{NDBC}}$ and $z_{0,\text{SAR}}$, obtained by using (22) with a $\gamma = 1.35$ and the parameters from the Takagaki schema, were compared in Fig. 7(a). The results revealed a strong correlation between

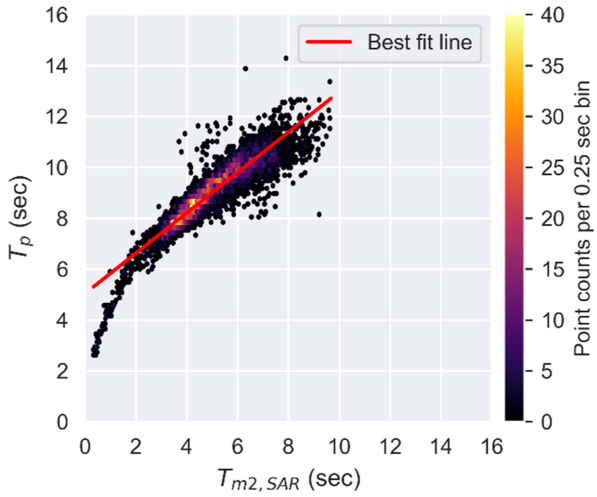


Fig. 5. Relationship of the optimized peak wave period ($T_p$) on the second moment wave period ( $T_{m2}$).

the computed values, with an RMSE of $0.04 \times 10^{-3}$ m, bias of $-0.01 \times 10^{-3}$ m, and *R* value of 0.97.

Fig 7(b) demonstrates the relationship between $\delta$ and $z_0$. $z_0$ demonstrates an increase with $\delta$ as it is proportional to $\delta$ raised to the power of three [$\beta = 3$ in (22)]. Fig. 7(a) and (b) demonstrates that many $z_0$ values appear to be larger than the constant value ( $z_0 = 0.2 \times 10^{-3}$ m), the recommended value in many articles [39].

Fig. 8 demonstrates the geographical distribution of the arithmetic average of $H_s$, $T_{m2}$, $T_p$, and $z_0$ from the validated SAR observations at the NDBC buoy's location. Fig. 8(a) shows that average $H_s$ ranging between 0.8 and 2.3 m. Fig. 8(b) demonstrates the average values of $T_{m2}$, with the highest values recorded in the Pacific and the lowest in the Gulf of Mexico. In addition, Fig. 8(c) presents $T_p$ based on the best-fit line equation in Fig. 5. Similar to $H_s$ and $T_{m2}$, it shows higher values of $T_p$

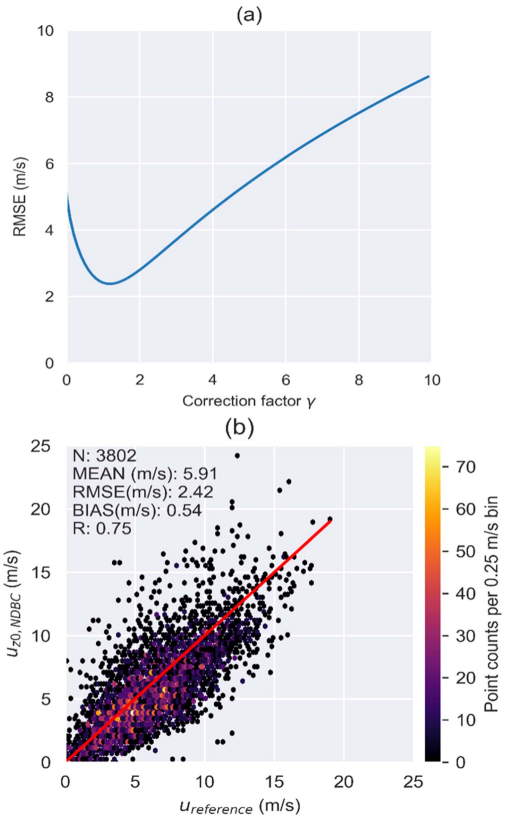


Fig. 6. (a) Correction factor ($\gamma$) which achieves the lowest RMSE of $u_{z0,\mathrm{NDBC}}$ vs. $u_{\mathrm{reference}}$ using Takagaki schema is 1.35. (b) $u_{z0,\mathrm{NDBC}}$ vs. $u_{\mathrm{reference}}$ after applying $\gamma = 1.35$.

in the Pacific region compared to other regions. The average $z_0$ values based on (22) are presented in Fig. 8(d). The map shows that the highest $z_0$ values were estimated in the Pacific region, especially for the buoys near the coast. Conversely, lower $z_0$ values were found in the Gulf of Mexico and some of the far offshore buoys.

## V. Discussion

### A. Sea State Parameters and Wind Speeds Derived From CWAVE_EX and CMOD5 Based on SAR IW

The validation results of the retrieved $H_s$ and $T_{m2}$ from SAR IW with a 10-m pixel spacing against in-situ measurements demonstrated the reliability of using this type of data in the coastal zones. The results also reveal more stable relationships between $H_s$ and in-situ measurements, in contrast to $T_{m2}$ with in-situ measurements. In comparison to wave height, wave period is a more complex variable. Even for near-zero waves (where SAR simply estimates amplitude, e.g., 15 cm $H_s$), $T_{m2}$ can range from 0 to 20 s. Most errors in period estimation typically occur in association with very low waves.

Furthermore, the comparison showed that these retrieved parameters correlated with their corresponding MFWAM–CMEMS model data. The MFWAM model is valuable as a complementary assessment of SAR-derived SSPs, and it has the advantage of spatial coverage compared with in-situ measurements. Pleskachevsky et al. [23] compared the MFWAM model data with the NDBC ocean observations for the buoy 46 001 in the western Gulf of Alaska. The comparison revealed a notable high correlation with RMSE of 26 cm. Therefore, comparing SAR SSPs with the CMEMS–MFWAM model further strengthens the trustworthiness of using SAR IW as an independent data source for wave observations.

Most of the collocated SAR observations were found for the ocean buoys located in the coastal zones less than 100 km from the coast, as the SAR IW data is acquired over lands and covers a limited buffer zone in the sea. Subsequently, few SAR observations were found for the very far offshore buoys, which could not help compare the performance of SAR IW in the open ocean against that of coastal zones.

Currently, a wide range of spaceborne SAR missions are available (e.g., TerraSAR-X, COSMO-Skymed, NovaSAR-1, ICEYE, and ALOS-2), which can produce SAR imagery with a very high spatial resolution. Using the strip map mode of TerraSAR-X (up to 3-m pixel spacing) can reduce the gap between the driven meteomarine parameters, wave models, and reference measurements up to 0.35 m [40].

Although sea state algorithms pose many challenges in the coastal zones due to the complex wave patterns, wave interaction with bathymetry, and land pixel contamination, the validation and comparison results of the CWAVE_EX algorithm demonstrated its reliability in the coastal zone. Thanks to the numerous features incorporated in the CWAVE_EX algorithm, which are in contrast to the original CWAVE designed for the open ocean. The CWAVE_EX was predominantly developed using coastal scenes from various regions, including the Baltic Sea, North Sea, Black Sea, Mediterranean Sea, Gulf of Alaska, and Hawaii. The subscene preparation steps aid in filtering out image artifacts, resampling, and denoising the subscenes utilized for SSPs retrieval. This implies that the retrieved SSPs originated from prefiltered and denoised subscenes.

Using other techniques, such as deep learning, can also reduce the uncertainties in SSPs, such as $H_s$ until 50%, as shown by [41].

These increased uncertainties at higher $H_s$ values, as presented in the time series of the ocean buoy 46 011 in Fig. 4, could be attributed to several factors. Environmental conditions, such as strong winds and rains, could influence SAR measurements, modifying the radar signal. In addition, wave breaking and complex wave patterns at high wave heights posed challenges in accurately estimating $H_s$. Pramudya et al. [42] have shown similarity with decreasing accuracy of $H_s$ under high wind speed and wind–wave dominant conditions. The ground truth uncertainty could be challenging in extreme wave conditions. Pleskachevsky et al. [21] showed a case in which the FINO platform suffered damage with a group of rough wave amplitudes exceeding 15 m, and the platform could not measure this event.

The current temporal resolution of S1 may not be sufficient to accurately represent the annual or seasonal variations of ocean waves. An increased number of SAR missions in space would improve the representativeness of samples. It enables a more comprehensive description of annual, seasonal, and diurnal wave patterns in coastal zones.

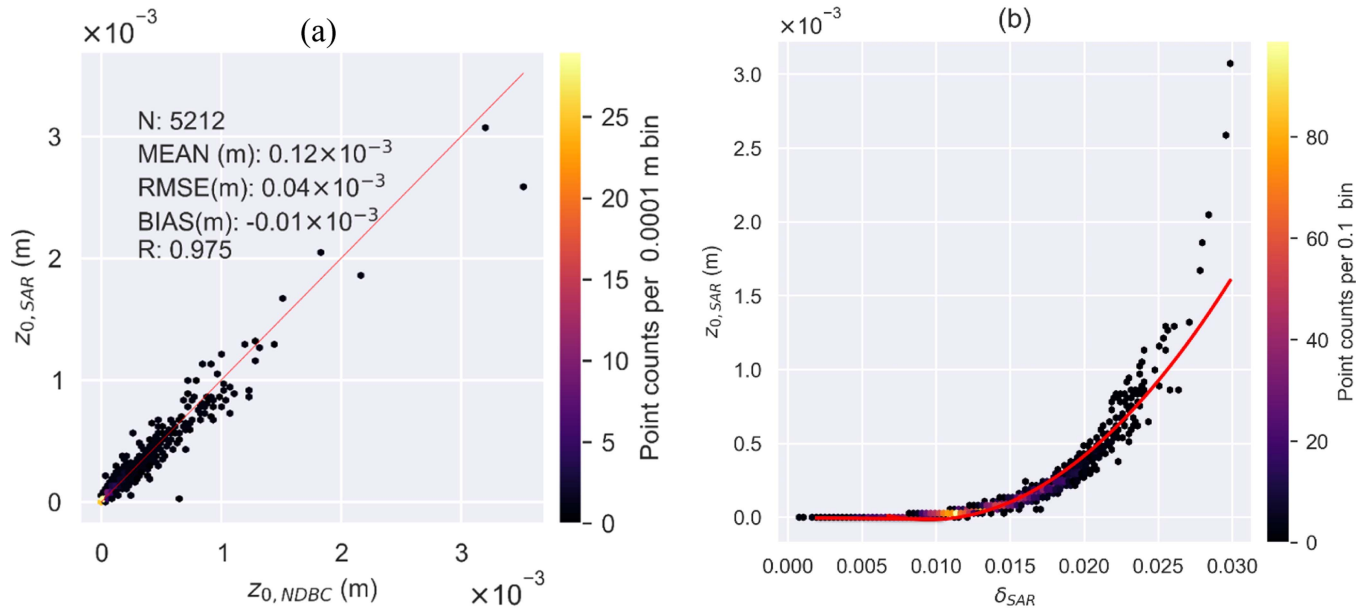


Fig. 7. (a) Roughness length comparison of $z_{0,\mathbf{SAR}}$ vs. $z_{0,\mathbf{NDBC}}$ using (22) with $\gamma = 1.35$, $\alpha$=10.94, and $\beta = 3$. (b) Wave steepness vs. $z_{0,\mathbf{SAR}}$.

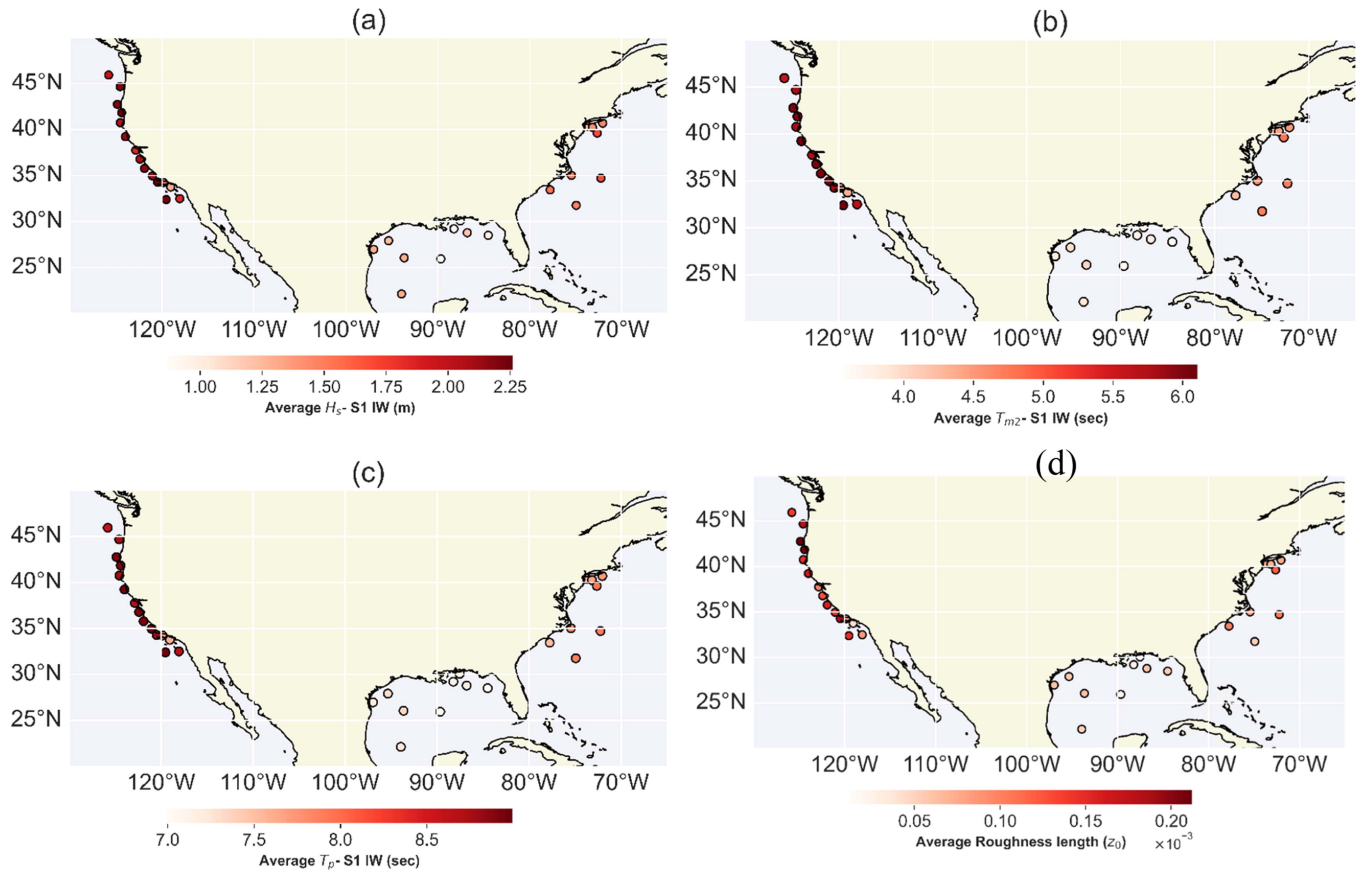


Fig. 8. Average meteo-marine parameters and wind from SAR: (a) Significant wave height ($\boldsymbol{H_s}$). (b) Second moment wave period ($\boldsymbol{T_{m2}}$). (c) Peak wave period ($\boldsymbol{T_p}$). (d) Average $z_{0,\mathbf{SAR}}$ based on modified Takagaki schema.

The validation results of $u_{\mathrm{SAR}}$ against in-situ measurements were consistent with other research studies that revealed the RMSE is $\sim$2 m/s or below and varying bias [43], [44], [45], [46]. In this article, CMOD5 was used to retrieve $u_{\mathrm{SAR}}$ and was previously derived to obtain stability-dependent wind speeds. An improved version of CMOD5 (CMOD5.N) can correct approximately 0.7 m/s in CMOD5. This correction encompasses 0.5 m/s, attributed to the bias in CMOD5, and an additional 0.2 m/s, which results from differences between non-neutral and neutral stability [25].

### B. Azimuthal Cutoff Length

The JONSWAP model was employed in this article to overcome the cutoff effects. The JONSWAP model has been widely adopted in various marine and coastal applications. It considers the influence of wind speed, duration, and fetch distance [see (4)–(6)]. The JONSWAP model was used to reproduce the frequency distribution of each given sea state using the CWAVE_EX algorithm. This representation helps to find the peak wave frequency of each sea state. The first check of the outcome of $T_p$, as it expected that $T_p$ is greater than $T_m$, is that the ratio of $T_p$ to $T_m(\frac{T_p}{T_{m2}})$ should greater than 1. This increment of $T_p$ is not unusual. As the most energetic wave component defines the peak period, it can experience sudden and sharp changes. In contrast, the whole ensemble of wave components evolving more smoothly determines the mean wave period. Previous articles have investigated the relation of $T_p$ with $T_m$. For example, Chun and Suh [47] have shown that $\frac{T_p}{T_{m2}}$ is 1.38. $T_p$ was used as an input to dispersion relation with water depth under the buoy to retrieve $L_p$, as illustrated in (17).

### C. Roughness Length Retrieval Based on Calibrated Takagaki Schema

The remarkable correlation of roughness length estimated based on SAR data $z_{0,\mathrm{SAR}}$ and buoys measurements $z_{0,\mathrm{NDBC}}$ emphasized the potential of leveraging SAR data for describing sea state variations and air–sea interaction as $z_0$ is the key parameter in the exchange of momentum between air and sea [17], [34].

The values of $z_0$ for some sea states, particularly with high wave steepness, is several times greater than the constant value of $z_0$ used in many applications. These findings further emphasize the importance of considering the variability of $z_0$ over the ocean in connection with model simulations, particularly in extreme wave conditions. This approach can be employed for the global mapping of $z_0$ based on SAR IW data considering the coastal effects of local variability in sea state.

The arithmetic mean of the samples represented the patterns of retrieved parameters. It has been found that the highest values, i.e., $H_s$ were found at the buoy locations in the Pacific region. Similarly, it was observed higher values for $H_s$ in the U.S. Pacific coastal areas are compared to other U.S. coastal areas using radar altimetry [48].

It is crucial to acknowledge that certain influential factors were not considered in $z_0$ variation in this article, such as the seabed's topographic features and wave age. It has been shown in Fig 8(d) that most of the highest average $z_0$ values are located close to the coastlines. Many articles have indicated that $z_0$ for coastal shallow water appears to differ from deep water [49]. More complicated mechanisms can modulate the waves than those encountered in the open waters [34]. Water depth plays a vital role in the interaction between waves and seabeds. The rough seabed with submerged ridges valleys can also modify the interaction of wave and seabed's features, subsequently leading to variation in $z_0$. Wave age is another aspect that was not explicitly considered in this article and can influence the characteristics of $z_0$. Younger waves tend to have higher $z_0$ compared with old waves [50].

## VI. Conclusion

This article explored the strengths and limitations of employing SAR S1 IW data to facilitate oceanic and atmospheric applications with SSPs and wind speeds, particularly in the coastal zones. Due to high satellite altitude and S1 IW SAR resolution data, SAR data inherently poses a considerable azimuthal cutoff length. The cutoff length poses a dilemma for retrieving the short wavelengths, which often exist in the coastal zones and are essential to retrieve $z_0$ through $H_s$ and $L_p$. Therefore, the JONSWAP model was introduced to overcome the limitation related to the azimuthal cutoff to retrieve additional physical parameters $f_p$ (or $T_p$) for each SAR collocation, which is needed to obtain the wavelengths using dispersion relation. After that, a novel approach is introduced to retrieve $z_0$ globally.

### A. Validation of $H_s$, $T_{m2}$, and $u_{\mathrm{SAR}}$

The validation results for $H_s$, $T_{m2}$ and $u_{\mathrm{SAR}}$, derived from SAR IW data through approximately 6000 collocations, exhibited a good agreement with buoy reference measurements with RMSE of 0.54 m, 1.28 s, and 2 m/s, respectively. This emphasizes the reliability of the data for diverse applications requiring wind and wave observations. $H_s$ relationship with in-situ measurements were more stable and better than $T_{m2}$. The time-series plot of one buoy, which had the highest collocation of observations, demonstrated high uncertainties in $H_s$ when wave heights were elevated.

In the comparison of $H_s$ and $T_{m2}$ with the hindcast CMEMS–MFWAM model, which involved about 380 000 collocations, the results indicated agreement with the RMSE of 0.46 m and 0.94 s, respectively.

Based on the retrieved SSPs, we observed higher values of $H_s$, $T_{m2}$, $T_p$, and $z_0$ in the Pacific region than in other regions. The likelihood of capturing the annual, seasonal, and diurnal variability is expected to increase with considerable SAR launches in space.

### B. Cutoff Effect Limitation By Sea State Imaging Process

The short $L_p$ ($<$135 m) is not retrievable by the CWAVE_EX algorithm directly due to cutoff effects. Introducing the JONSWAP model gives insight into $f_p$ (or $T_p$) of each SSP. The ratio of $T_p$ to $T_{m2}$ was about 1.5. This ratio is verified and found

to fall within the expected range of ratios, consistent with other research outcomes that suggest the fact that $T_p$ is higher than $T_{m2}$. $L_p$ was retrieved using dispersion relation with water depth and $T_p$ as $L_p$ is a fundamental parameter to estimate $z_0$ based on $\delta$.

### C. Roughness Length Retrieval Based on SAR

The estimated $z_0$ values from SAR-derived SSPs and ocean buoys strongly correlate with RMSE of $0.04 \times 10^{-3}$ m and bias of $-0.01 \times 10^{-3}$ m. This presented approach can provide global information about $z_0$ thanks to the global coverage of SAR. Our results revealed significant variability in $z_0$ from the Pacific to the Atlantic and the Gulf of Mexico.

The temporal resolution of SAR data should be enhanced to further utilize SSPs for offshore wind energy applications. It can be achieved by increasing the number of SAR constellations in space. Using a higher resolution of SAR data will improve the reliability of obtained SSPs and $z_0$. In addition, it reduces the azimuthal cutoff length.

In this article, we parametrized $z_0$ based on $\delta$, highlighting the importance of using this approach in extreme wave conditions or higher wind speeds. These conditions cause more perturbation of the sea surface, leading to high $z_0$. Other crucial factors are influential and can impact $z_0$, such as water depth, seabed topography, and wave age.

On this account, it is highly recommended to investigate the impact of $\delta$ on NRCS values and quantify the RMSE variation of wind data at different sites in our study areas based on variation on $\delta$.

## Author Contributions

**Abdalmenem Owda**: Conceptualization, Methodology, Investigation, Writing—original draft. **Andrey Pleskachevsky**: Methodology (CWAVE_EX and wave part), review & editing. **Xiaoli Guo Larsén**, **Merete Badger**, **Dalibor Cavar**, **Charlotte Hasager**: Review and editing.

## Data Availability

S1 mission data (1 level GRDH) is available at https://scihub.copernicus.eu/dhus/#/home (last access: 19th February 2023) and https://search.asf.alaska.edu/#/?center = −97.494,39.673&zoom = 3.000 (last access: 19th February 2013). Buoys measurements are available at https://www.ndbc.noaa.gov/ (access: 19th February 2023).

GLORYS12V1 product is the CMEMS global ocean eddy-resolving reanalysis covering altimetry (1993 onward) (10.48670/moi-00021).

## Acknowledgment

The main author is grateful to the LAB Bremen team and the lab head, Sven Jacobsen. The authors are thankful to Otto Mønsted Fonden for covering half the expenses of the visiting research. We thank ESA and NOAA for providing public access to data from S-1A/B and buoy measurements. XG acknowledges support from GASPOC and MAMAS projects. We sincerely thank the anonymous reviewers and editors for their valuable feedback and suggestions for improving the article.

## References

[1] A. Pleskachevsky, S. Jacobsen, B. Tings, and E. Schwarz, "Estimation of sea state from Sentinel-1 synthetic aperture radar imagery for maritime situation awareness," *Int. J. Remote Sens.*, vol. 40, no. 11, pp. 4104–4142, 2019, doi: 10.1080/01431161.2018.1558377.

[2] F. Ardhuin et al., "Observing sea states," *Front. Mar. Sci.*, vol. 6, 2019, Art. no. 124, doi: 10.3389/fmars.2019.00124.

[3] R. C. Ramachandran, C. Desmond, F. Judge, J.-J. Serraris, and J. Murphy, "Floating offshore wind turbines: Installation, operation, maintenance and decommissioning challenges and opportunities," *Wind Energy Sci.*, vol. 7, no. 2, pp. 903–924, 2022, doi: 10.5194/wes-2021-120.

[4] A. Pleskachevsky, D. Velotto, and S. Jacobsen, "Meteo-marine parameters and their variability observed by high resolution satellite radar images," *Oceanography*, vol. 26, no. 2, pp. 80–91, 2013, doi: 10.5670/oceanog.2013.36.

[5] A. L. Pleskachevsky, W. Rosenthal, and S. Lehner, "Meteo-marine parameters for highly variable environment in coastal regions from satellite radar images," *ISPRS J. Photogrammetry Remote Sens.*, vol. 119, pp. 464–484, 2016, doi: 10.1016/j.isprsjprs.2016.02.001.

[6] S. Rikka, A. Pleskachevsky, S. Jacobsen, V. Alari, and R. Uiboupin, "Meteo-marine parameters from Sentinel-1 SAR imagery: Towards near real-time services for the Baltic Sea," *Remote Sens.*, vol. 10, no. 5, 2018, Art. no. 757, doi: 10.3390/rs10050757.

[7] F. Collard, F. Ardhuin, and B. Chapron, "Extraction of coastal ocean wave fields from SAR images," *IEEE J. Ocean. Eng.*, vol. 30, no. 3, pp. 526–533, Jul. 2005, doi: 10.1109/JOE.2005.857503.

[8] J. Sun and H. Kawamura, "Retrieval of surface wave parameters from SAR images and their validation in the coastal seas around Japan," *J. Oceanogr.*, vol. 65, pp. 567–477, May 2009.

[9] J. Schulz-Stellenfleth, T. König, and S. Lehner, "An empirical approach for the retrieval of integral ocean wave parameters from synthetic aperture radar data," *J. Geophys. Res. Oceans*, vol. 112, no. 3, Mar. 2007, Art. no. C03019, doi: 10.1029/2006JC003970.

[10] B. Djath, J. Schulz-Stellenfleth, and B. Cañadillas, "Study of coastal effects relevant for offshore wind energy using spaceborne synthetic aperture radar (SAR)," *Remote Sens.*, vol. 14, no. 7, Apr. 2022, Art. no. 1688, doi: 10.3390/rs14071688.

[11] D. Myrhaug, B. J. Leira, and W. Chai, "Application of a sea surface roughness formula using joint statistics of significant wave height and spectral wave steepness," *J. Ocean Eng. Mar. Energy*, vol. 6, no. 1, pp. 91–97, Feb. 2020, doi: 10.1007/s40722-020-00160-0.

[12] S. Porchetta et al., "Evaluation of a roughness length parametrization accounting for wind–wave alignment in a coupled atmosphere–wave model," *Quart. J. Roy. Meteorol. Soc.*, vol. 147, no. 735, pp. 825–846, Jan. 2021, doi: 10.1002/qj.3948.

[13] S. Porchetta et al., "A new roughness length parameterization accounting for wind-wave (mis)alignment," *Atmos. Chem. Phys.*, vol. 19, no. 10, pp. 6681–6700, 2019, doi: 10.5194/acp-19-6681-2019.

[14] W. H. Munk, "Wind stress on water: A hypothesis," *Quart. J. Roy. Meteorol. Soc.*, vol. 81, no. 350, pp. 639–639, 1955, doi: 10.1002/qj.49708135026.

[15] X. Larsén et al., *Extreme Winds and Waves for Offshore Turbines: Coupling Atmosphere and Wave Modeling for Design and Operation in Coastal Zones*, vol. 154. DTU Library, Oct. 2017. [Online]. Available: https://backend.orbit.dtu.dk/ws/portalfiles/portal/139272513/FinalReport_PSO12020_XWiWa_20171031.pdf

[16] P. A. Jiménez and J. Dudhia, "On the need to modify the sea surface roughness formulation over shallow waters," *J. Appl. Meteorol. Climatol.*, vol. 57, no. 5, pp. 1101–1110, 2018, doi: 10.1175/JAMC-D-17-0137.1.

[17] P. K. Taylor and M. J. Yelland, "The dependence of sea surface roughness on the height and steepness of the waves," *J. Phys. Oceanogr.*, vol. 31, no. 2, pp. 572–590, 2001, doi: 10.1175/1520-0485(2001)031<0572:TDOSSR>2.0.CO;2.

[18] W. Alpers and C. Rufenach, "The effect of orbital motions on synthetic aperture radar imagery of ocean waves," *IEEE Trans. Antennas Propag.*, vol. 27, no. 5, pp. 685–690, Sep. 1979.

[19] R. Zhang et al., "Influence of radar parameters and sea State on wind wave-induced velocity in C-band ATI SAR ocean surface currents," *Remote Sens.*, vol. 14, no. 17, Sep. 2022, Art. no. 4135, doi: 10.3390/rs14174135.

[20] F. Ardhuin et al., "Semiempirical dissipation source functions for ocean waves. Part I: Definition, calibration, and validation," *J. Phys. Oceanogr.*, vol. 40, no. 9, pp. 1917–1941, 2010, doi: 10.1175/2010JPO4324.1.
[21] A. L. Pleskachevsky, S. Lehner, and W. Rosenthal, "Storm observations by remote sensing and influences of gustiness on ocean waves and on generation of rogue waves," *Ocean Dyn.*, vol. 62, no. 9, pp. 1335–1351, Sep. 2012, doi: 10.1007/s10236-012-0567-z.
[22] G. R. Valenzuela, "Theories for the interaction of electromagnetic and oceanic waves—A review," *Boundary Layer Meteorol.*, vol. 13, no. 1–4, pp. 61–85, 1978, doi: 10.1007/BF00913863.
[23] A. Pleskachevsky, B. Tings, S. Wiehle, J. Imber, and S. Jacobsen, "Multi-parametric sea state fields from synthetic aperture radar for maritime situational awareness," *Remote Sens. Environ.*, vol. 280, 2022, Art. no. 113200, doi: 10.1016/j.rse.2022.113200.
[24] "ESA manual," 2014. [Online]. Available: https://sentinels.copernicus.eu/web/sentinel/radiometric-calibration-of-level-1-products
[25] H. Hersbach, A. Stoffelen, and S. De Haan, "An improved C-band scatterometer ocean geophysical model function: CMOD5," *J. Geophys. Res. Oceans*, vol. 112, no. 3, pp. 1–18, 2007, doi: 10.1029/2006JC003743.
[26] K.-F. Dagestad et al., "Wind retrieval from synthetic aperture radar—An overview," in *Proc. 4th SAR Oceanogr. Workshop*, 2012, p. 22.
[27] A. Pleskachevsky, S. Wiehle, J. Imber, and S. Jacobsen, "Remote sensing of environment multiparametric sea state fields from synthetic aperture radar for maritime situational awareness," *Remote Sens. Environ.*, vol. 280, Oct. 2022, Art. no. 113200, doi: 10.1016/j.rse.2022.113200.
[28] Y. Wan, X. Zhang, Y. Dai, L. Li, and X. Qu, "Azimuth cutoff compensation method for SAR wave observation based on multiview wave spectrum data fusion," *IEEE Access*, vol. 8, pp. 120923–120935, 2020, doi: 10.1109/ACCESS.2020.3006244.
[29] B. Holt, "SAR imaging of the ocean surface," in *SAR Marine User's Manual*, C.R. Jackson and J.R. Apel Eds. NOAA/NESDIS Office of Research and Applications. [Online]. Available: https://www.sarusersmanual.com/
[30] K. Hasselmann et al., "Measurements of wind-wave growth and swell decay during the joint North Sea wave project (JONSWAP)," Deutsches Hydrographisches Institut, Hamurge, 1973.
[31] J. E. Stopa, A. A. Mouche, B. Chapron, and F. Collard, "Sea state impacts on wind speed retrievals from C-band radars," *IEEE J. Sel. Topics Appl. Earth Observ. Remote Sens.*, vol. 10, no. 5, pp. 2147–2155, May 2017, doi: 10.1109/JSTARS.2016.2609101.
[32] H. Shan, C. Dong, and J. Liang, "Deep-sea research part II influence of sea surface wave-dependent roughness on summer precipitation over the Southeastern United States," *Deep-Sea Res. Part II*, vol. 206, Apr. 2022, Art. no. 105209, doi: 10.1016/j.dsr2.2022.105209.
[33] D. Sun, J. Song, X. Li, K. Ren, and H. Leng, "A novel sea surface roughness parameterization based on wave state and sea foam," *J. Mar. Sci. Eng.*, vol. 9, no. 3, pp. 1–25, 2021, doi: 10.3390/jmse9030246.
[34] Y. He, J. Fu, P. W. Chan, Q. Li, Z. Shu, and K. Zhou, "Reduced sea-surface roughness length at a coastal site," *Atmosphere*, vol. 12, no. 8, 2021, Art. no. 991, doi: 10.3390/atmos12080991.
[35] J. R. Garratt, "Review of drag coefficients over oceans and continents," *Amer. Meteorol. Soc.*, vol. 105, pp. 915–929, 1977.
[36] B. Liu, C. Guan, and L. Xie, "The wave state and sea spray related parameterization of wind stress applicable from low to extreme winds," *J. Geophys. Res. Oceans*, vol. 117, no. 7, pp. 1–11, 2012, doi: 10.1029/2011JC007786.
[37] F. Anctil and M. A. Donelan, "Air–water momentum flux observations over shoaling waves," *J. Phys. Oceanogr.*, vol. 26, pp. 1344–1353, 2015.
[38] N. Takagaki et al., "Strong correlation between the drag coefficient and the shape of the wind sea spectrum over a broad range of wind speeds," *Geophys. Res. Lett.*, vol. 39, no. 23, pp. 1–6, 2012, doi: 10.1029/2012GL053988.
[39] D. Saheb, M. Koussa, and S. Hadji, "Technical and economical study of a stand-alone wind energy system for remote rural area electrification in Algeria," *Renewable Energy Power Qual. J.*, vol. 1, no. 12, pp. 638–643, 2014, doi: 10.24084/repqj12.439.
[40] S. Rikka, A. Pleskachevsky, R. Uiboupin, and S. Jacobsen, "Sea state in the Baltic Sea from space-borne high-resolution synthetic aperture radar imagery," *Int. J. Remote Sens.*, vol. 39, no. 4, pp. 1256–1284, Feb. 2018, doi: 10.1080/01431161.2017.1399475.
[41] B. Quach, Y. Glaser, J. E. Stopa, A. A. Mouche, and P. Sadowski, "Deep learning for predicting significant wave height from synthetic aperture radar," *IEEE Trans. Geosci. Remote Sens.*, vol. 59, no. 3, pp. 1859–1867, Mar. 2021, doi: 10.1109/TGRS.2020.3003839.
[42] F. S. Pramudya, J. Pan, and A. T. Devlin, "Estimation of significant wave height of near-range traveling ocean waves using Sentinel-1 SAR images," *IEEE J. Sel. Topics Appl. Earth Observ. Remote Sens.*, vol. 12, no. 4, pp. 1067–1075, Apr. 2019, doi: 10.1109/JSTARS.2019.2902566.
[43] T. Ahsbahs, M. Badger, P. Volker, K. S. Hansen, and C. B. Hasager, "Applications of satellite winds for the offshore wind farm site Anholt," *Wind Energy Sci.*, vol. 3, no. 2, pp. 573–588, 2018, doi: 10.5194/wes-3-573-2018.
[44] T. Ahsbahs, G. MacLaurin, C. Draxl, C. R. Jackson, F. Monaldo, and M. Badger, "US East Coast synthetic aperture radar wind atlas for offshore wind energy," *Wind Energy Sci.*, vol. 5, no. 3, pp. 1191–1210, 2020, doi: 10.5194/wes-5-1191-2020.
[45] Y. Lu, B. Zhang, W. Perrie, A. A. Mouche, X. Li, and H. Wang, "A C-band geophysical model function for determining coastal wind speed using synthetic aperture radar," *IEEE J. Sel. Topics Appl. Earth Observ. Remote Sens.*, vol. 11, no. 7, pp. 2417–2428, Jul. 2018, doi: 10.1109/JSTARS.2018.2836661.
[46] L. Zhou et al., "Sea surface wind speed retrieval from textures in synthetic aperture radar imagery," *IEEE Trans. Geosci. Remote Sens.*, vol. 60, Mar. 2021, Art. no. 4200911, doi: 10.1109/TGRS.2021.3062401.
[47] H. Chun and K. D. Suh, "Estimation of significant wave period from wave spectrum," *Ocean Eng.*, vol. 163, pp. 609–616, Feb. 2018, doi: 10.1016/j.oceaneng.2018.06.043.
[48] M. Passaro, M. A. Hemer, G. D. Quartly, C. Schwatke, D. Dettmering, and F. Seitz, "Global coastal attenuation of wind-waves observed with radar altimetry," *Nat. Commun.*, vol. 12, no. 1, 2021, Art. no. 3812, doi: 10.1038/s41467-021-23982-4.
[49] Z. Gao, Q. Wang, and M. Zhou, "Wave-dependence of friction velocity, roughness length, and drag coefficient over coastal and open water surfaces by using three databases," *Adv. Atmos. Sci.*, vol. 26, no. 5, pp. 887–894, 2009, doi: 10.1007/s00376-009-8130-7.
[50] J. A. P. Veiga and M. R. Queiroz, "Impact of the waves on the sea surface roughness length under idealized like-hurricane wind conditions (Part II)," *Atmos. Climate Sci.*, vol. 05, no. 03, pp. 326–335, 2015, doi: 10.4236/acs.2015.53025.

**Abdalmenem Owda** received the B.Eng. degree in civil engineering from the Birzeit University, Birzeit, Palestine, in 2012, and the M.Sc. degree in geomatics engineering from the University of Stuttgart, Stuttgart, Germany, in 2016.

He has 5 years of experience with photogrammetry and remote sensing applications. He was employed as a Ph.D. student with the Department of Wind and Energy Systems, Technical University of Denmark, Kongens Lyngby, Denmark, until 2024. He is currently working as Postdoc researcher in Atmospheric remote sensing, at the Remote Sensing Technology Institute, German Aerospace Center, Oberpfaffenhofen Munich. His research interests include using remote sensing observations for offshore wind farms and coastal applications.

**Andrey Pleskachevsky** received the diploma degree in hydropower engineering from the Technical University St. Petersburg, St. Petersburg, Russia, in 1994, focusing on hydrodynamic numerical modeling and data analyses.

His Ph.D. was performed with the GKSS-Research Center (today Helmholtz Center HERION), where he worked on spectral wave modeling and coupling of waves, circulation, and suspended matter transport models, as well as the implementation of satellite data into modeling until 2009. In 2009, he joined the Remote Sensing Technology Institute, German Aerospace Center, Cologne, Germany, where he develops algorithms for retrieval of the meteomarine parameters from synthetic aperture radar for near-real-time services.

**Xiaoli Guo Larsén** received the Ph.D. degree in marine boundary layer meteorology from the Uppsala University, Uppsala, Sweden, in 2003.

She is currently a Full Professor with the Department of Wind and Energy Systems, Technical University of Denmark, Kongens Lyngby, Denmark. She has 20 years of experience in wind energy, specifically for wind resources and siting conditions. Her research interests include extreme winds and storms, wind-wave coupled modeling, and cross-scale atmospheric turbulence.

**Merete Badger** received the B.Sc., M.Sc., and Ph.D. degrees in physical geography from the Department of Geography, University of Copenhagen, Copenhagen, Denmark, in 1999, 2002, and 2006, respectively.

She has 20 years of experience with applications of Earth Observation for wind energy. She was employed with the Department of Wind and Energy Systems, Technical University of Denmark, Kongens Lyngby, Denmark, until 2023, and she is currently affiliated with the Copenhagen Business School, Frederiksberg, Denmark. Her research interests include mapping winds and wind resources over the ocean using synthetic aperture radar, and she has authored/coauthored extensively about this topic.

**Dalibor Cavar** received the M.Sc. and Ph.D. degrees in mechanical engineering and fluid mechanics from the Technical University of Denmark (DTU), Kongens Lyngby, Denmark, in 2002 and 2006, respectively.

Since past 20 years, he has been working with various aspects of computational fluid dynamics (CFD) related to wind engineering. He is currently working as a Senior Scientist with the Wind Energy and Energy Systems Department, DTU. His research interests include advanced approaches to turbulence modeling, CFD computations of atmospheric boundary layer flows, including canopy and atmospheric stability effects, as well as the coupling of mesoscale and microscale numerical models.

**Charlotte Bay Hasager** (Member, IEEE) received the M.Sc. degree in physical geography from the University of Copenhagen, Copenhagen, Denmark, in 1992, and the Ph.D. degree in remote sensing and climatology from the University of Copenhagen, in 1996.

She has been employed with the Risø National Laboratory, Roskilde, Denmark, since 1993, and with the Technical University of Denmark, Roskilde, Denmark, since 2007. She is currently a Full Professor with the Department of Wind and Energy Systems, Technical University of Denmark, Risø Campus, Roskilde, Denmark. She works in the section on Meteorology and Remote Sensing. Her research interests include offshore wind energy meteorology, satellite remote sensing, synthetic aperture radar and other Earth observing instruments, and ground-based remote sensing for wind and precipitation.